GEM NEWS INTERNATIONAL

Contributing Editors
Gagan Choudhary, *IIGJ-Research & Laboratories Centre, Jaipur, India* (gagan.choudhary@iigjrlc.org)
Christopher M. Breeding, *GIA, Carlsbad* (christopher.breeding@gia.edu)
Guanghai Shi, *School of Gemmology, China University of Geosciences, Beijing* (shigh@cugb.edu.cn)

Figure 1. The 9.63 ct pink grossular garnet reportedly from Mogok (A) fluoresced very strong red under long-wave UV (B) and weak chalky red under short-wave UV radiation (C). Photos by Qian Zhang.

COLORED STONES AND ORGANIC MATERIALS

Grossular with strong red fluorescence. The authors recently encountered a pink garnet rough reportedly from Mogok, Myanmar. The garnet was characterized by a light pink color in daylight, and it showed unusual strong red fluorescence under long-wave ultraviolet radiation and a weak chalky red reaction under short-wave UV (figure 1). A previously published report on grossular garnet showed similar fluorescence under long-wave UV, but the short-wave UV reaction was very different (M.S. Krzemnicki, "Pink grossular garnet from Mogok," *Facette*, No. 26, 2020, pp. 26).

Raman spectroscopy identified the garnet as grossular. Electron probe microanalysis determined that the composition was consistent with that of nearly pure grossular with major elements of calcium, aluminum, and silicon ($Ca_{3.114}Al_{2.003}Si_{2.883}O_{11.885}$), and laser ablation–inductively coupled plasma–mass spectrometry (LA-ICP-MS) testing revealed trace elements of titanium, vanadium, manganese, and others (table 1). The pink coloration was due to two weak bands between 470 and 600 nm in the UV/visible absorption spectrum; Geiger et al. (1999) suggested they are related to Mn^{3+} (C.A. Geiger et al., "Raspberry-red grossular from Sierra de Cruces Range, Coahuila, Mexico," *European Journal of Mineralogy*, Vol. 11, No. 6, 1999, pp. 1109–1113).

A photoluminescence spectrum recorded with 325 nm laser excitation displayed a strong narrow band at 604 nm accompanied by some weaker bands at 583, 595, 617, 631, 645, and 660 nm (figure 2). Gaft et al. (2013, 2022) pub-

Editors' note: Interested contributors should send information and illustrations to Stuart Overlin at soverlin@gia.edu.

Gems & Gemology, Vol. 58, No. 4, pp. 508–526.

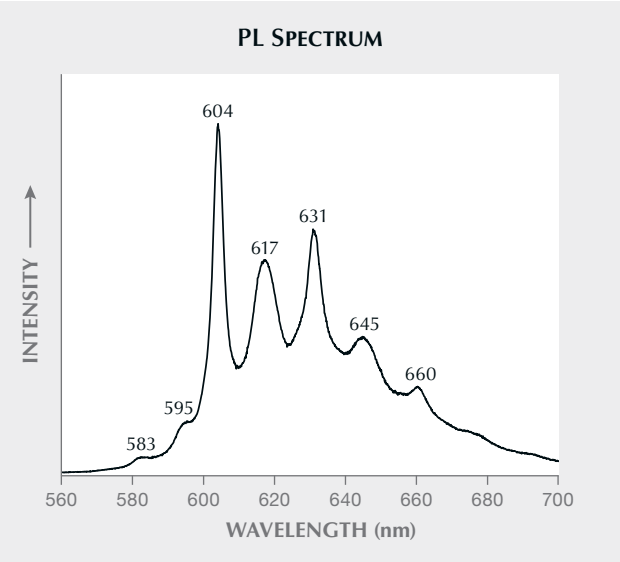

Figure 2. The photoluminescence spectrum collected on the grossular using 325 nm excitation at 300 K.

lished two papers about the luminescence of grossular (M. Gaft et al., "Laser-induced time resolved luminescence of natural grossular $Ca_3Al_2(SiO_4)_3$," *Journal of Luminescence*, Vol. 137, 2013, pp. 43–53; M. Gaft et al., "Zero-phonon Mn^{2+} luminescence in natural grossular $Ca_3Al_2(SiO_4)_3$," *Journal of Luminescence*, Vol. 248, 2022, article no. 119001). Our result is consistent with their 2022 result. They proposed that such luminescence emission may be related to the presence of Mn^{2+}.

In order to describe the pink grossular fluorescence features in detail, 3D fluorescence spectral data (i.e., excitation-emission mapping or EEM) was collected at room temperature using a Jasco FP-8500 fluorescence spectrometer (figure 3). The excitation wavelengths varied from 350 to 630 nm, with a step size of 1 nm and an excitation bandwidth of 5 nm. The emission spectra were collected from 400 to 680 nm, with the bandwidth set to 2.5 nm and a data interval of 0.1 nm, showing five obvious emission wavelengths at 604, 617, 631, 645, and 660 nm and their corresponding optimal excitation wavelength at 388 nm.

To our knowledge, this is the first time a detailed fluorescence analysis of pink grossular has been documented.

Qian Zhang and Andy H. Shen
Gemmological Institute,
China University of Geosciences, Wuhan

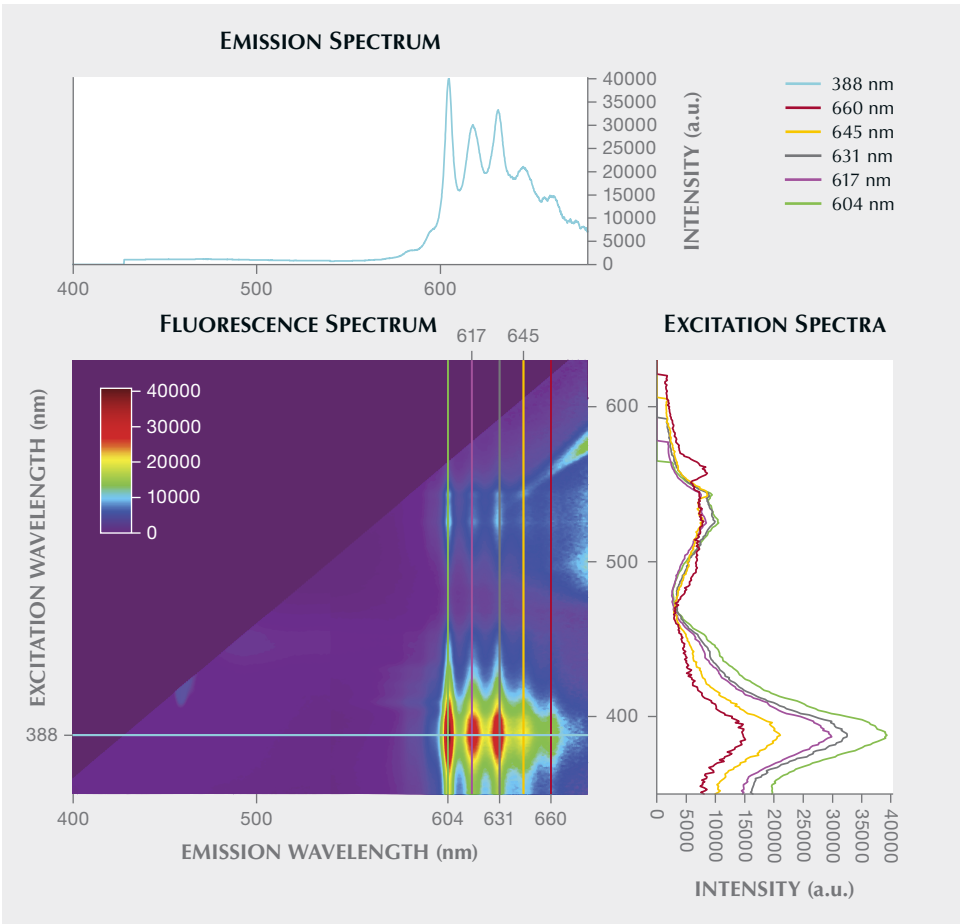

Figure 3. The 3D contour map of the pink grossular's fluorescence spectrum. The stacked excitation spectra are not scaled or shifted for clarity.

TABLE 1. LA-ICP-MS trace element chemistry (in ppmw) of the pink grossular.

	Ti	V	Cr	Mn	Fe	Nb	Sn	Nd
Spot 1	272	10.8	8.50	66.4	30.9	85.2	16.7	0.21
Spot 2	226	12.4	8.09	61.8	48.9	96.1	10.5	0.71
Spot 3	219	12.8	bdl[a]	59.4	bdl	97.1	10.3	0.39
Spot 4	265	9.05	bdl	66.0	35.3	83.4	16.5	0.19
Spot 5	280	9.06	6.31	67.5	bdl	75.9	21.2	0.34
Detection limits	1.58	0.15	4.21	1.68	23.70	0.07	1.31	0.16

[a]*bdl: below detection limit*

Extremely rare hellandite inclusion found in a Mogok ruby. Recently, Guild Gem Laboratories (Shenzhen) received a 0.45 ct ruby (figure 4) for origin determination. Standard gemological testing, including a refractive index of 1.762–1.770 and specific gravity of approximately 4.00, and Fourier-transform infrared spectroscopy confirmed its identity as corundum. Additionally, energy-dispersive X-ray fluorescence revealed extremely low iron (247 ppmw) and relatively high chromium (3819 ppmw) and vanadium (448 ppmw) concentrations, consistent with those in marble-hosted samples.

Microscopic observation showed a typical inclusion scene for Burmese ruby from Mogok, including nested concentrations of fine, long to short rutile needles (figure 5) and irregular calcite crystals (figure 6). To our surprise, two transparent brownish crystals (figure 7) were observed. Their slightly corroded state indicated these crystal inclusions' protogenetic origin. Micro-Raman spectroscopy using 473 nm laser excitation produced some interesting results. Raman analysis showed several distinct peaks at 207, 238, 298, 317, 349, 423, 475, 574, 793, 868, 987, and 1018 cm^{-1}, consistent with those of hellandite according to the RRUFF database (figure 8; see B. Lafuente et al., 2015, https://rruff.info/about/downloads/HMC1-30.pdf). These hellandite inclusions are rarely observed in ruby from any origin.

Hellandite, a rare borosilicate mineral with the proposed ideal formula of $(Ca, REE)_4(Y, Ce)_2Al_2(B_4Si_4O_{22})(OH)_2$, comes in various colors, including colorless, brown, brownish red, gray, green, and yellow. First found in granitic pegmatite in Norway, hellandite belongs to the

Figure 4. This 0.45 ct oval-shaped ruby, measuring 4.25 × 3.65 × 3.24 mm, exhibited a highly saturated red color. Photo by Huixin Zhao.

Figure 5. Dense, nested concentrations of silk in the ruby suggest an origin of Mogok, Myanmar. Photomicrograph by Huixin Zhao; field of view 1.13 mm.

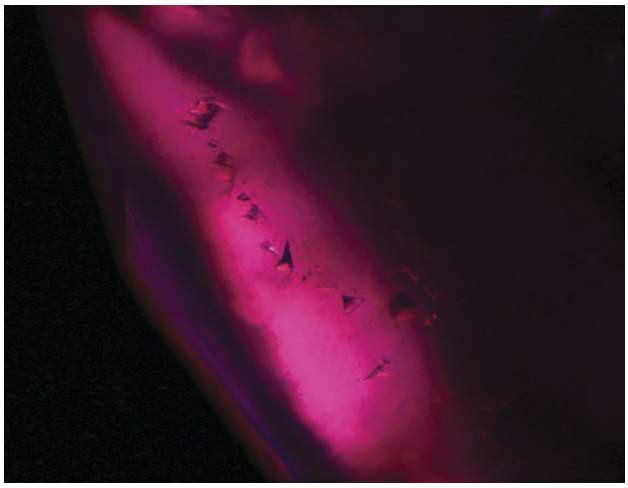

Figure 6. A series of irregular calcite crystals in the ruby from Mogok. Photomicrograph by Huixin Zhao; field of view 1.84 mm.

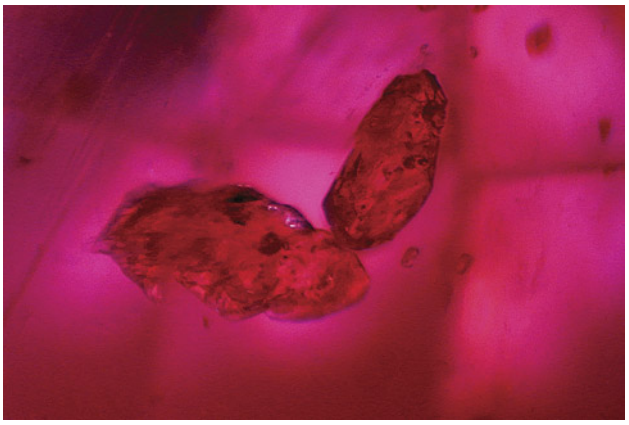

Figure 7. These two transparent brownish hellandite crystals found in a Mogok ruby possibly represent a new ruby inclusion. Photomicrograph by Huixin Zhao; field of view 1.70 mm.

monoclinic crystal system. Its crystal structure was determined on a specimen from Predazzo, Italy, and described as $B_4Si_4O_{22}$ chains parallel to the *c*-axis (M. Mellini and S. Mellini, "Hellandite: A new type of silicoborate chain," *American Mineralogist*, Vol. 62, No. 1-2, 1977, pp. 89–99).

Myanmar's ruby deposits occur in marbles intercalated with gneisses that are sometimes intruded by granitoids (G. Giuliani and L.A. Groat, "Geology of corundum and emerald gem deposits: A review," Winter 2019 *G&G*, pp. 464–489). Therefore, we speculate that hellandite crystals

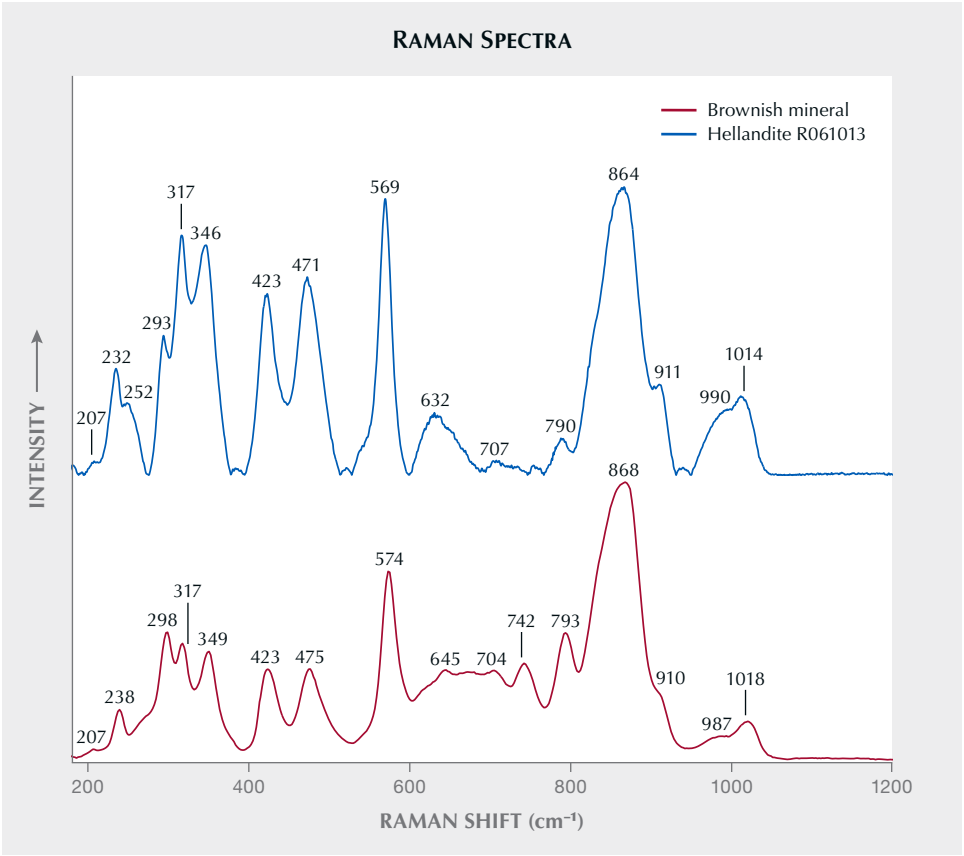

Figure 8. Raman analysis identified the two transparent brownish crystals shown in figure 7 as hellandite. Spectra are offset for clarity.

Figure 9. This bangle, weighing 40.10 g, was identified as quartzite. Photo by Su Xu.

in the granitoids intruding gneiss were captured by ruby when the ruby formed.

To our knowledge, this is the first time hellandite has been observed in ruby. This finding allows for a better understanding of included minerals in the ruby from the geological setting of the Mogok mine.

Xueying Sun, Yujie Gao (peter.gao@guildgemlab.com), and Qi Han
Guild Gem Laboratories, Shenzhen

Quartzite bangle with fuchsite inclusions. Jadeite jade bangles are always popular in the Chinese market. With high prices and rising demand for these products, a bangle with an appearance similar to jadeite was encountered recently.

The bangle was submitted to the National Gold-Silver Gem & Jewelry Quality Inspection Center (Sichuan) for identification. It was semitransparent with a white and green bodycolor resembling that of jadeite (figure 9). However, standard gemological testing showed a refractive index of 1.54 and a specific gravity of 2.67, values that were both significantly below those of jadeite and more in line with quartz. It showed no reaction under Chelsea filter. Using a polariscope, the material was found to be composed of polycrystalline aggregates. Microscopic examination revealed a granular aggregate structure and different microcrystalline mineral inclusions.

The identity was further confirmed by analytical testing. Fourier-transform infrared (FTIR) reflectance spectroscopy showed peaks at 489, 537, 691, 778, 798, 1105, and 1178 cm^{-1} that were consistent with the characteristic spectrum of quartzite (sometimes referred to as "quartzose") (figure 10) (X. Jin et al., "Gemmological and vibrational spectrum characteristics of micaceous quartzose jade 'strawberry crystal'," *Journal of Gems & Gemmology*, Vol. 23, No. 3, 2021, pp. 20–28). Energy-dispersive X-ray fluorescence (EDXRF) analysis revealed trace amounts of iron throughout and chromium exclusive to the green inclusions.

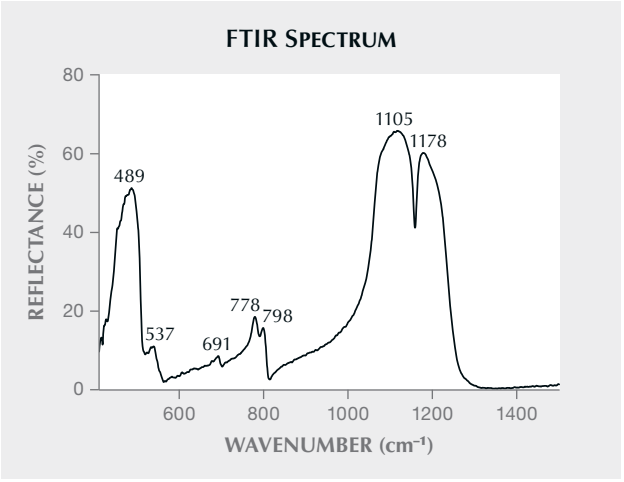

Figure 10. The bangle's infrared reflectance spectrum exhibited characteristic peaks at 489, 537, 691, 778, 798, 1105, and 1178 cm^{-1} that are typical for quartzite.

These green flaky inclusions were slightly oriented. Raman combined with EDXRF analysis identified them as fuchsite ($K(Al,Cr)_2(AlSi_3O_{10})(OH)_2$), a green chromium-colored variety of muscovite (figure 11A) (Fall 2013 GNI, pp. 183–184). Additionally, brassy yellow inclusions in a range

Figure 12. The UV-Vis spectrum of the green area showed two broad absorption bands centered at 423 and 600 nm in addition to a weak peak at 684 nm, indicating the presence of chromium.

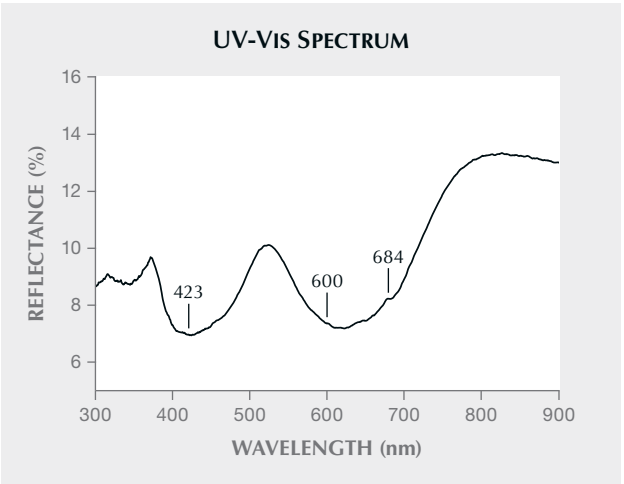

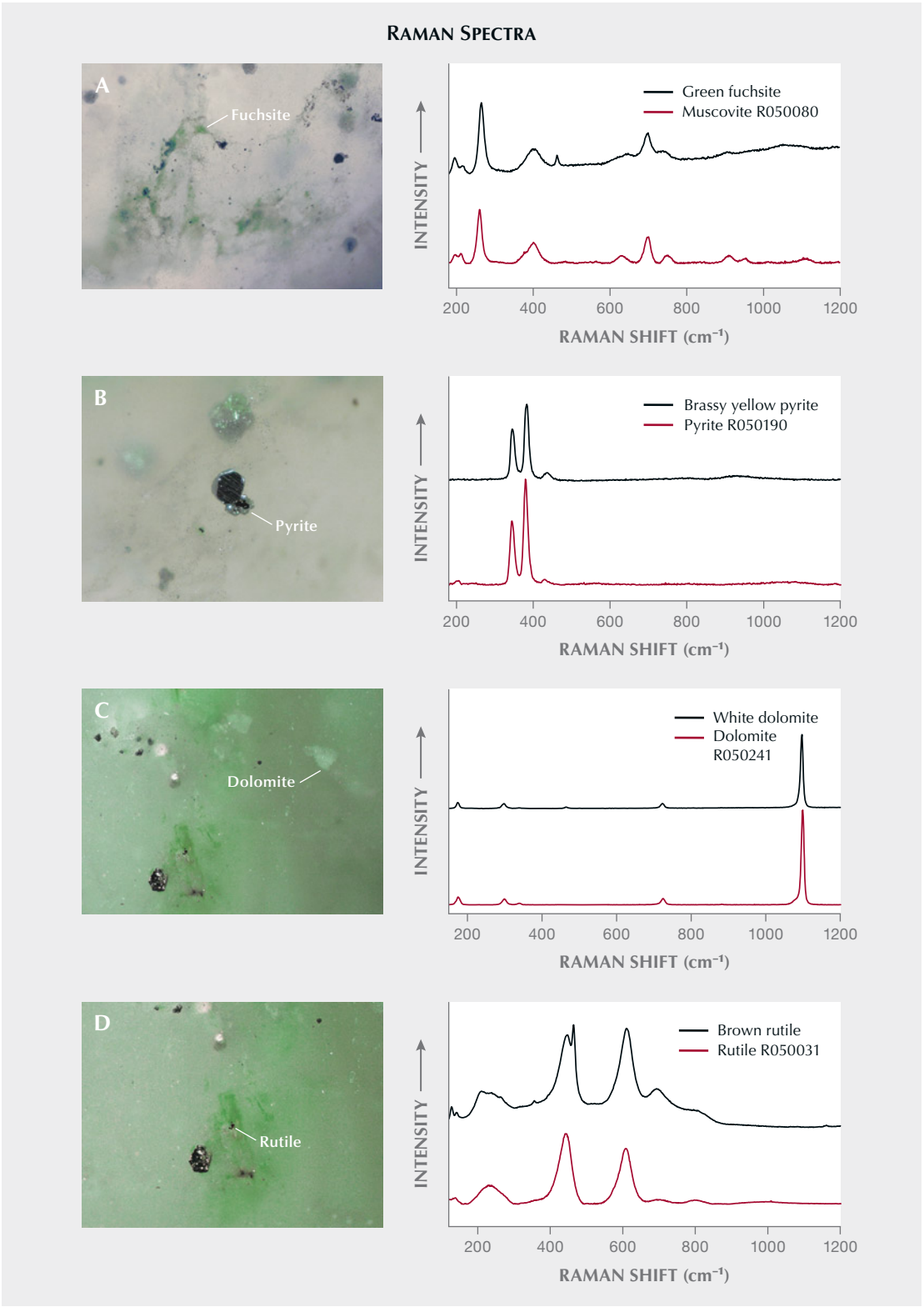

Figure 11. Photomicrographs and Raman spectra of inclusions in the bangle (black) and the reference spectrum in the RRUFF database (red): flaky fuchsite (A), brassy yellow pyrite (B), white dolomite (C), and brown rutile (D), shown in darkfield illumination (A) and reflected light (B–D). Photomicrographs by Su Xu; fields of view 0.2 mm (A), 1 mm (B), 0.8 mm (C), and 0.05 mm (D). See B. Lafuente et al. (2015), https://rruff.info/about/downloads/HMC1-30.pdf. Spectra are offset vertically for clarity.

Figure 13. Left to right: Reconstructed root amber (assembled from small fragments and from powders), natural Burmese root amber, and plastic imitation. Photos by Yilei Feng.

of sizes were confirmed as pyrite (figure 11B) using Raman spectroscopy. Raman also identified some white blocky inclusions in a nearby area as dolomite (figure 11C), as well as some tiny brown rutile inclusions found as irregular, randomly scattered grains (figure 11D).

Ultraviolet/visible spectroscopy corresponding to the green areas showed two broad absorption bands at about 423 and 620 nm, with a weak peak at 684 nm (figure 12). These features have been assigned to Cr^{3+} in fuchsite.

To our knowledge, fuchsite contained in quartzite is usually uniformly scattered in the form of tiny flakes. The uneven distribution of green fuchsite that resulted in patches of green in this bangle is noteworthy. The patchy green spots resemble the color concentrations often observed in jadeite. Despite the bangle's resemblance to jadeite, gemological tests such as refractive index, microscopic observation, and infrared and Raman spectroscopy readily identify it.

Su Xu
National Gold-Silver Gem & Jewelry Quality Inspection Center, Sichuan
Xiaoping Shi
Sichuan Provincial Coal Design & Research Institute

SYNTHETICS AND SIMULANTS

Identification of natural, reconstructed, and imitation root amber. Natural root amber is a variety of Burmese amber with a distinct appearance, good luster, and deep color (Y. Wang, *Amber Gemology*, China University of Geosciences Press, Beijing, 2018, p. 145). Root amber was named for its similarity in color and structure to tree roots. Root amber beads are popular in the Chinese market, and the Guangzhou Gemstone Testing Center receives many of them for identification. Recently we have noticed three different types submitted for identification (figures 13 and 14): natural root amber, reconstructed root amber (assembled from either pressed powders or small fragments), and plastic imitations.

Specific gravity (SG) was measured for three natural Burmese root amber samples (N-1 through N-3), three samples reconstructed from pressed powders (M-1 through M-3), three samples reconstructed from pressed fragments (M-4 through M-6), and three plastic imitations (P-1 through P-3). The SG of most varieties of regular Burmese amber samples is within 1.020–1.050, except for root amber and reddish amber (1.060–1.110). Overall, the natural root amber had higher SG (1.044–1.107) than that of regular Burmese amber and much lower SG than that of the reconstructed root amber from pressed amber powders (1.133–1.137) and plastic imitations (1.161–1.167). The root amber reconstructed from pressed fragments, meanwhile, had an SG of 1.075–1.077. The variations in SG of the reconstructed amber were due to differences in internal structure and/or gas porosity.

Most importantly, the internal features of the samples were quite different. There were some cellular or porous structures in the natural Burmese root amber (figure 15A). The typical red-brown dots of Burmese amber could be detected in both transparent and opaque zones (figure 15B). The flow-like pattern of natural Burmese root amber can be lamellar, annular, or flocculent, and there are natural tran-

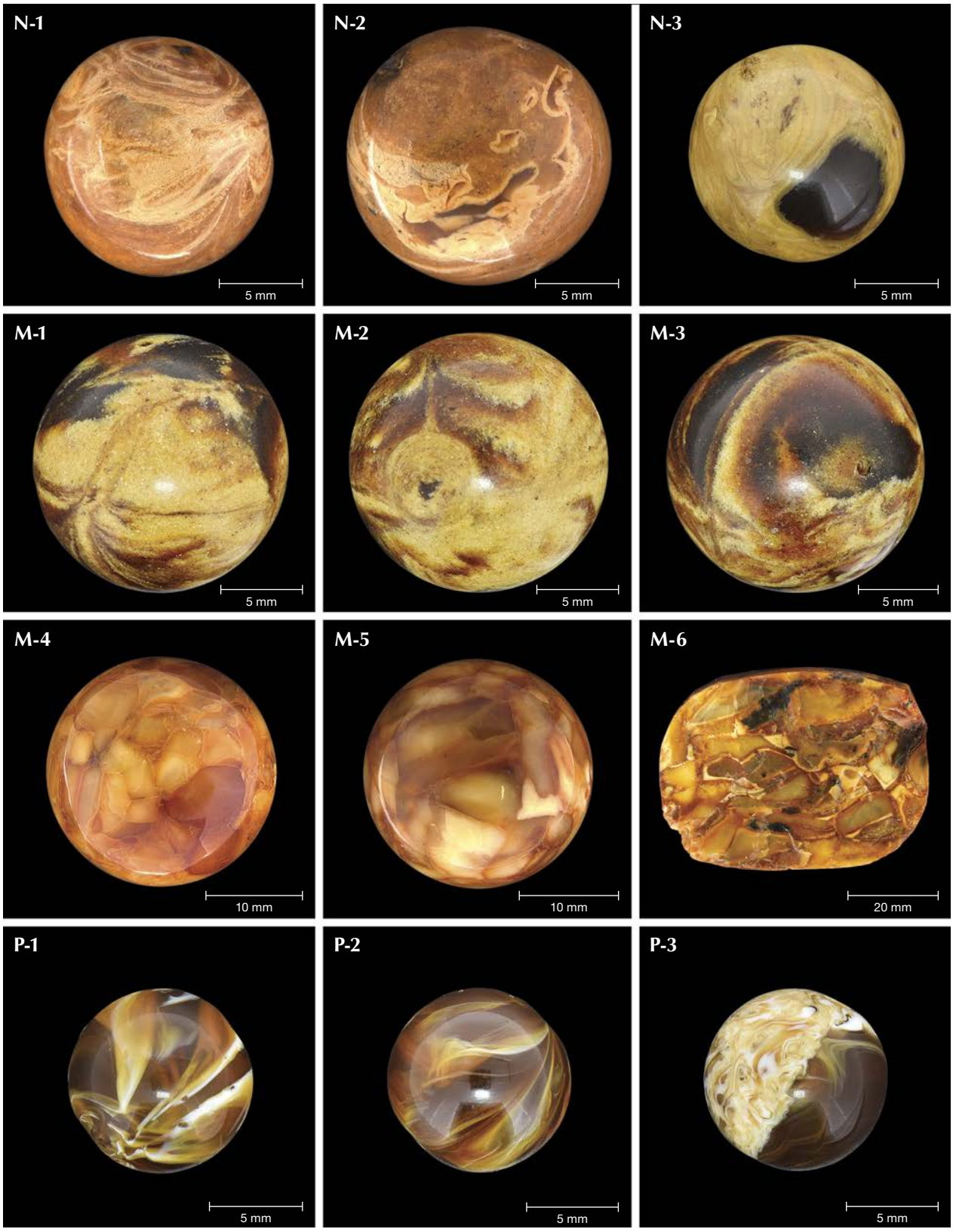

Figure 14. Natural Burmese root amber beads (N-1 through N-3), root amber beads reconstructed from pressed amber powders (M-1 through M-3) and small fragments (M-4 through M-6), and plastic root amber imitations (P-1 through P-3). Photos by Yilei Feng and Zhaoyi Li.

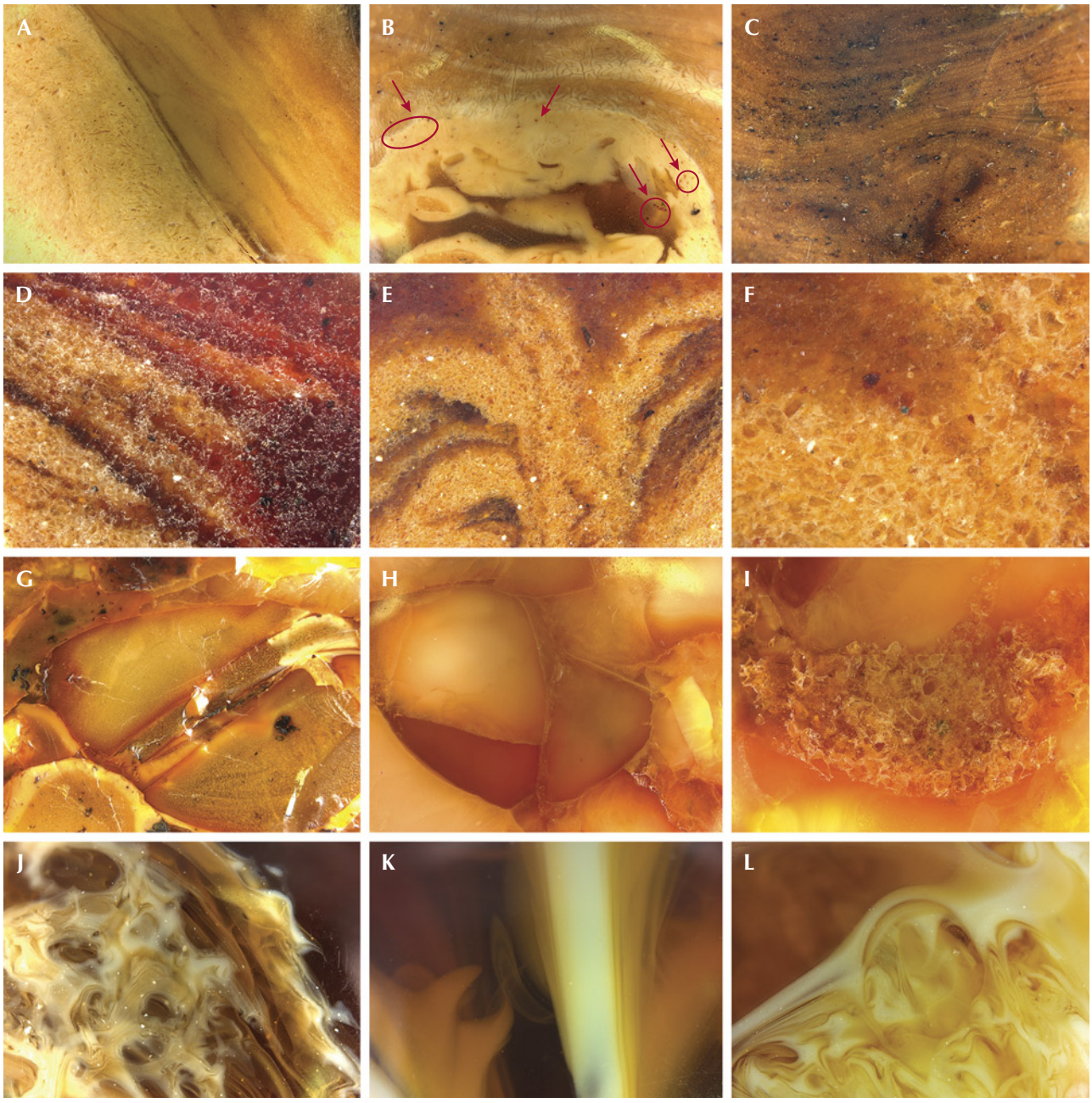

Figure 15. Row 1: Internal features of natural Burmese root amber beads: cellular or porous structures (A), red-brown dots in both transparent and opaque zones (B), and the lamellar flow-like pattern with a natural color transition (C). Row 2: Root amber beads reconstructed from pressed amber powders: a flow-like pattern formed by an accumulation of powders (D and E) and a granular texture (F). Row 3: Root amber beads reconstructed from small fragments of pressed amber: clear and rigid borders of the fragments (G and H) and a small granular texture seen in a larger patch structure (I). Row 4: Plastic root amber imitations showing ribbon-, string-, or ring-like patterns (J–L, respectively). Photomicrographs by Yilei Feng and Zhaoyi Li. Fields of view: 10.6 mm (A), 9.0 mm (B), 5.6 mm (C), 2.80 mm (D), 10.4 mm (E), 7.7 mm (F), 11.3 mm (G), 10.7 mm (H), 9.3 mm (I), 5.6 mm (J), 5.0 mm (K), and 4.9 mm (L).

sitions between varying colors (figure 15C). The internal features of the root amber reconstructed from pressed powders displayed an unnatural flow-like pattern similar to the veins of a leaf (figure 15, D–E). Under higher magnification, these

samples displayed a granular texture (a sugar- or sand-like pattern with apparent broken particles), confirming that small amber micro-particles had been pressed (figure 15F). There were very clear and rigid borders in the root amber reconstructed from fragments (figure 15, G and H). Some granular texture could still be found in these samples (figure 15I). The flow-like pattern of plastic imitation is mostly ribbon-, string-, or ring-like, with a sense of separation between the brown matrix and the obvious boundaries (figure 15, J–L).

Using Fourier-transform infrared (FTIR) spectroscopy, the plastic imitations were quickly identified in the mid-infrared range (3500–500 cm^{-1}). The extremely strong peak at 1731 cm^{-1}, three peaks of increasing intensity (1240, 1192, and 1148 cm^{-1}), and other peaks suggest that the material is an amino resin (figure 16, blue line). The vibration peaks of functional groups of natural root amber mainly appear at 2928, 2860, 1720, 1458, 1375, 1227, 1141, 1028, and 974 cm^{-1}, consistent with the main FTIR peaks of Burmese amber (figure 16, green line). The obvious "Baltic shoulder" (Y. Wang et al., "Characteristics of hydrothermally treated beeswax amber," Fall 2019 *G&G*, pp. 370–387), composed of a broad and weak absorption shoulder at 1265 cm^{-1} and a sharp peak at 1158 cm^{-1} as well as an absorption peak near 887 cm^{-1}, appeared in two reconstructed root amber specimens (figure 16, pink and purple lines). It can be inferred that these two reconstructed samples were pressed from rough Baltic amber.

Yan Li, Yilei Feng, and Zhaoyi Li
Gemmological Institute,
China University of Geosciences, Wuhan

Yamei Wang
Gemmological Institute,
China University of Geosciences, Wuhan
Guangzhou Gemstone Testing Center,
China University of Geosciences, Wuhan

Synthetic rock crystal quartz cluster with natural-looking inclusions. A client recently submitted for identification the piece shown in figure 17, assuming it to be a natural mineral specimen. It weighed 1114 g, measured 119 × 126 mm, and contained colorless transparent to semitransparent crystals. Eye-visible inclusions as well as numerous tiny crystals and some minute powdered material were seen around the cluster's base.

Standard gemological testing yielded a refractive index of 1.542–1.555, a specific gravity of 2.65, and inert reactions under long- and short-wave UV radiation, properties consistent with quartz. Microscopic examination revealed obvious fluid and two-phase inclusions (figure 18). Examination by

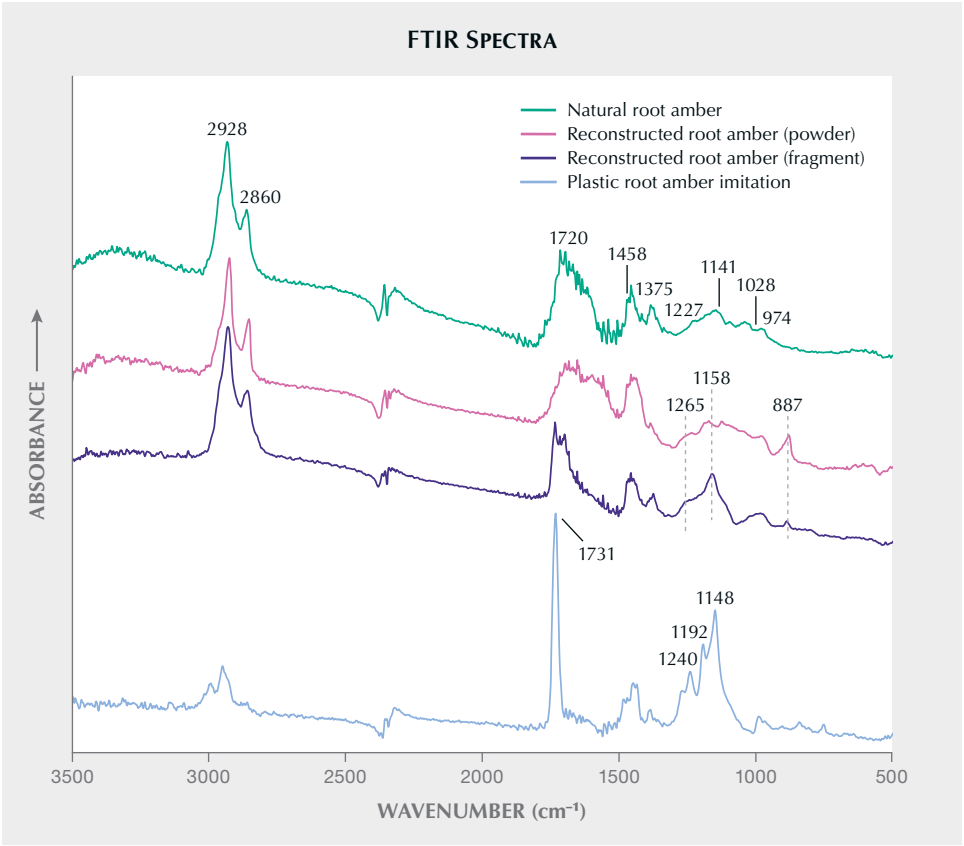

Figure 16. FTIR spectra of natural, reconstructed, and imitation root amber in the mid-infrared range (3500–500 cm^{-1}). Spectra are offset vertically for clarity.

Figure 17. The cluster specimen weighing 1114 g and measuring 119 × 126 mm. Photo by Lai Tai-An Gem Lab.

Fourier-transform infrared (FTIR) spectroscopy showed an absorbance region in the 400–1600 cm^{-1} range, also consistent with quartz, and Raman spectroscopy confirmed the identification. However, the most important data came from the FTIR analysis in transmission mode in the 1000–6000 cm^{-1} range. A characteristic peak of synthetic quartz at 3584 cm^{-1} (figure 19) was observed, while peaks consistent with natural quartz (3378, 3482, and 3595 cm^{-1}) were not detected. Similar spectra were collected from the other crystals in the group, confirming a synthetic origin (S. Karampelas et al., "Infrared spectroscopy of natural vs. synthetic amethyst: An update," Fall 2011 *G&G*, pp. 196–201; Winter 2015 Lab Notes, pp. 439–440).

Figure 18. Magnification revealed obvious fluid and two-phase inclusions within the crystals. Photomicrograph by Lai Tai-An Gem Lab; field of view 4.60 mm.

Synthetic quartz crystal clusters are not new to the market, but as the use of synthetic quartz has increased, such crystal specimens have become available on numerous online shopping platforms. Surprisingly, most of them are sold as "natural quartz clusters." One of the common trade methods for separating natural and synthetic quartz clusters is to observe the striations on the prism faces. In natural quartz, the striations form horizontally (perpendicular to the *c*-axis), while synthetic quartz typically displays diagonal or triangular striations (figure 20) (Winter 2016

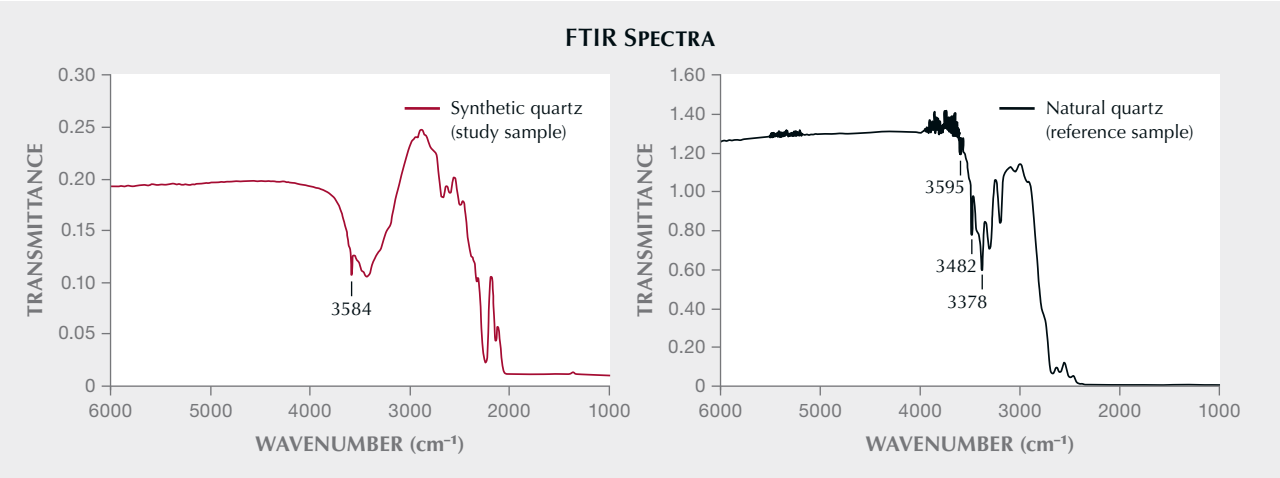

Figure 19. A peak at 3584 cm^{-1} in the FTIR spectrum proved the rock crystal quartz specimen was synthetic (red). In contrast, a natural quartz reference sample analyzed by our lab exhibits peaks at 3378, 3482, and 3595 cm^{-1} (black) that were absent in the sample.

G&G Micro-World, pp. 425–426). This method may aid in identification but should not be considered diagnostic, since the striations can be faked.

When synthetic quartz clusters are fashioned into polished products, the potential of misidentifying them as "natural quartz" increases significantly, especially with inexperienced consumers and small-scale labs lacking analytical equipment. In such cases, the inclusion scene is almost identical to that observed in natural quartz, and the helpful prismatic face growth lines disappear. Therefore, members of the trade should be cautious when handling synthetic quartz, although the crystal clusters may be somewhat easier to identify.

Larry Tai-An Lai (laitaiangemlab@gmail.com)
Lai Tai-An Gem Laboratory, Taipei

Red-dyed spodumene imitating ruby. A semitranslucent deep red oval faceted gem, measuring 13.88 × 9.08 × 5.88 mm and weighing 5.72 ct (figure 21), was recently submit-

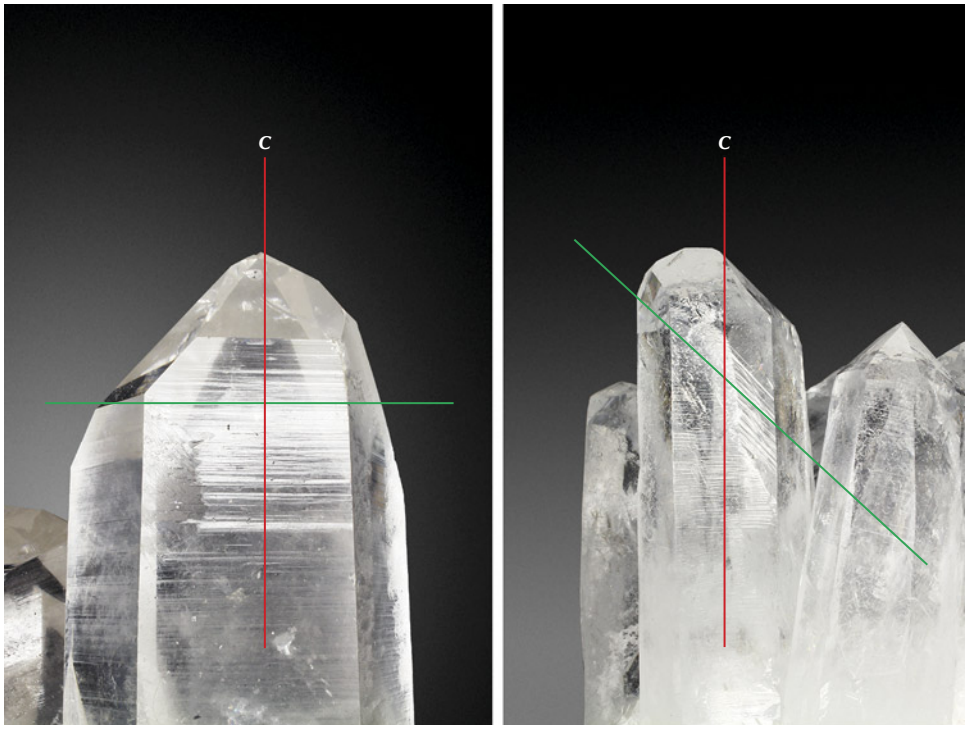

Figure 20. Natural quartz's horizontal prismatic striations, relative to the c*-axis (left, reference sample), were instead diagonal in the synthetic quartz cluster studied (right). Because striations can be faked, they should not be considered diagnostic. Photos by Lai Tai-An Gem Lab.*

Figure 21. A semitranslucent 5.72 ct red-dyed spodumene, presented as "red corundum." Photo by Guy Borenstein.

ted to Stuller Inc. by a client for a custom design. The stone was presented as "red corundum." But initial quality control testing showed a biaxial refractive index of 1.659–1.678 with a birefringence of 0.019, which did not correspond with corundum.

Due to the incorrect identity, the stone was sent to Stuller's gemological laboratory for further analysis. Standard gemological testing revealed a specific gravity of 3.237, with a moderate orange reaction to long-wave UV and a very weak reaction, along the fractures, to short-wave UV, typical of spodumene species. Further analysis, using a 532 nm Raman laser, also provided well-matched results for spodumene ($LiAl(SiO_3)_2$). Although the collected results clearly pointed to spodumene, the deep red color it displayed was questionable and required further investigation.

Unpolarized ultraviolet/visible/near-infrared (UV-Vis-NIR) spectroscopy showed two merging broad bands centered at 530 and 561 nm (figure 22). The former is probably associated with the Mn^{3+} chromophore (H.U. Rehman et al., "An X-ray absorption near-edge structure (XANES) study on the oxidation state of chromophores in natural kunzite samples from Nuristan, Afghanistan," *Minerals*, Vol. 10, No. 5, 2020, article no. 463), while the latter was previously reported as associated with red dyeing (K. Schmetzer et al., "Dyed natural corundum as a ruby imitation," Summer 1992 *G&G*, pp. 112–115). A possibly iron- and manganese-related shoulder at 430 nm (R. Lu, "Color origin of lavender jadeite: An alternative approach," Winter 2012 *G&G*, pp. 273–283) was also observed.

Fourier-transform infrared (FTIR) spectroscopy revealed peaks at 2954, 2924, 2872, and 2854 cm^{-1} (figure 23), typical of a universal paraffin oil filler (M.L. Johnson et al., "On the identification of various emerald filling substances," Summer 1999 *G&G*, pp. 82–107; L. Kiefert et al., "Identification of filler substances in emeralds by infrared and Raman spectroscopy," *Journal of Gemmology*, Vol. 26, No. 8, 1999, pp. 501–520). Under deep UV illumination (<225 nm), the foreign filler in the surface-reaching fractures fluoresced strongly pink while the spodumene host rock was inert. The effect was especially prominent in a cavity near the girdle (figure 24).

Microscopic examination verified the FTIR, UV-Vis-NIR, and deep UV findings and revealed surface-reaching cleavages and fractures filled with a red foreign substance (figure 25), as well as natural inclusions.

The recorded results confirmed the gem as a red-dyed spodumene. Although spectroscopy identified some manganese, the lack of pink/red reaction under deep UV suggests a low concentration (Lu, 2012). Therefore, the authors assume that the starting material was either colorless or very pale pink spodumene.

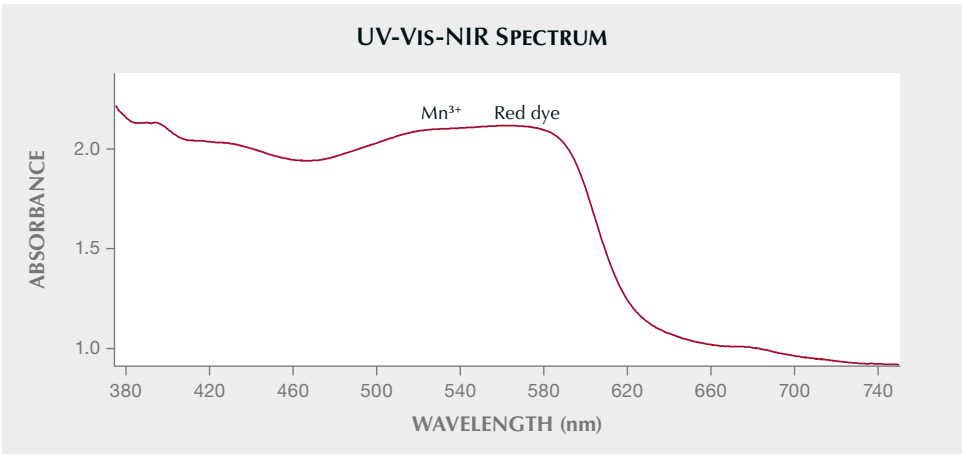

Figure 22. The unpolarized UV-Vis-NIR spectrum of the dyed spodumene shows a broad band centered at 561 nm due to the red dye. The band centered at 430 nm may be related to an intervalence charge transfer species between neighboring iron and manganese, while the band at 530 nm may be related to Mn^{3+}.

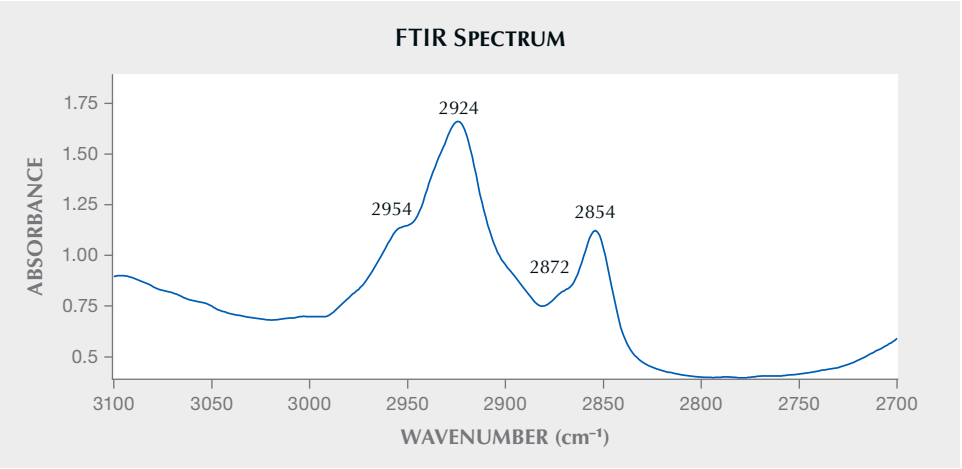

Figure 23. The FTIR spectrum of the dyed spodumene shows a series of peaks at 2954, 2924, 2872, and 2854 cm^{-1}, associated with a typical universal paraffin oil.

Introducing red dye to intensify the color of corundum is a longstanding practice (Schmetzer et al., 1992). To the best of our knowledge, however, this is the first time a spodumene has been treated with a colored oil to imitate ruby. The result masks the true identity of the gem, and without gemological testing, an uneducated trader could misidentify it as a color-enhanced ruby.

Guy Borenstein and Sean O'Neal
Stuller Inc.
Lafayette, Louisiana

CONFERENCE REPORT

GSA 2022 annual meeting. The Geological Society of America (GSA) held its annual meeting October 9–12 in Denver, Colorado. GIA's tenth technical session, entitled "Gemological Research in the Twenty-First Century—Gem Materials and Localities," featured twelve oral presentations and five posters (figure 26), covering broad topics including diamond, sapphire, tourmaline, sunstone, nephrite, and other gem materials.

Colored Gemstones and Other Subjects. The session started with recent research on colored gemstones. **Dr. Peter Heaney** (Pennsylvania State University, State College) opened with a keynote presentation addressing the structural coloration in colored gemstones that is produced by micro- or nano-structures. This structural coloration results from the interference of nanoparticle inclusions with light waves, including film interference, diffraction grating, scattering, and photonic crystals. Nanoparticles were characterized by a variety of techniques, including scanning electron microscopy (SEM), focused ion beam (FIB), transmission electron microscopy (TEM), and atomic force microscopy (AFM). Dr. Heaney summarized his group's state-of-the-art

Figure 24. Deep UV imaging of the spodumene's surface showed strong luminescence of the dye within a cavity as well as surface-reaching fractures. Image by Guy Borenstein; field of view 6.25 mm.

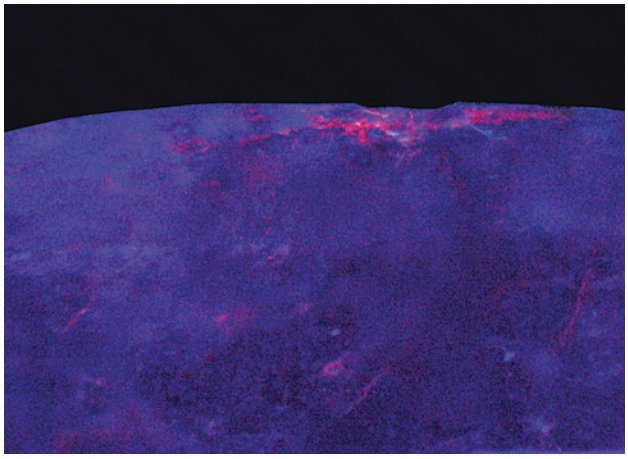

Figure 25. Color concentration within surface-reaching fractures confirmed dye treatment in the spodumene. Photomicrograph by Guy Borenstein; field of view 2.66 mm.

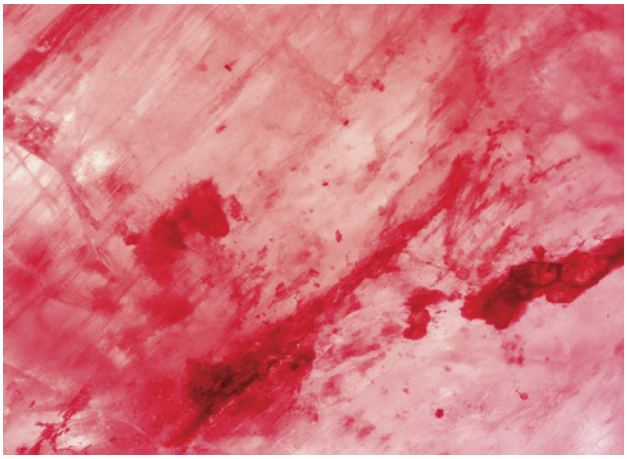

Figure 26. GSA 2022 oral and poster presenters. Left to right: Elina Myagkaya, Shiyun Jin, Che Shen, Stephanie Persaud, Roy Bassoo, Rhiana Henry, Alexander Goodsuhm, Rachelle Turnier, Yusuke Katsurada, Mei Yan Lai, Matthew Hardman, Christopher Breeding, Evan Smith, and Peter Heaney. Photo by Robert Weldon.

research on iridescent gemstones, including three-dimensional photonic arrays of hematite (Fe_2O_3) nanoneedles, quasi-periodic void layers in goethite (FeOOH), blazed gratings of Brazil twinning in iridescent quartz, and hierarchical oscillation layers in iris agate. Continuing with the topic of structural colorization, **Dr. Shiyun Jin** (GIA, Carlsbad) investigated the cause of special colors (green, red, and watermelon) and the optical effects of pleochroism in Oregon sunstone. The absorption and scattering power of copper nanoparticles in sunstone was tested with experimental absorption/scattering spectra and modeling based on Maxwell's equations. By comparing his experimental results and simulations, Dr. Jin concluded that the metallic copper nanoparticles in Oregon sunstone absorb and scatter incident light differently with respect to light polarization, thus yielding various color effects. **Che Shen** (Munsell Color Science Laboratory, Rochester Institute of Technology) studied the color change in sapphire caused by varying the amounts of six major chromophores (V^{3+}, Cr^{3+}, Fe^{3+}, Fe^{2+}-Ti^{4+}, h-Cr^{3+}, and h-Fe^{3+}). Using chromatic adaptation transformation (CAT), the color of sapphire under daylight and incandescent light were modeled by combining various chromophores. Shen concluded that blue/purple sapphire is caused by Fe^{2+}-Ti^{4+} and Cr^{3+}, green/reddish brown sapphire by Fe^{2+}-Ti^{4+} and Fe^{3+}, and pink/purplish brown sapphire by Fe^{2+}-Ti^{4+}, Cr^{3+}, and Fe^{3+}.

Figure 27. Aaron Palke presented the various types of melt inclusions in Montana's secondary sapphire. James Shigley (seated) moderated the session. Photo by Robert Weldon.

Other oral presentations focused on sapphire formation. **Dr. Aaron Palke** (GIA, Carlsbad) investigated the multiple types of melt inclusions in Montana's secondary sapphire, especially silica-rich felsic, sulfide, and polycrystalline melts (figure 27). The presence of multiple types of melt inclusions indicates that these sapphires are of magmatic origin. Further research on Montana sapphire by **Alexander Goodsuhm** (GIA, Carlsbad) constrained the formation conditions for Montana sapphire using zircon concentrations in rutile inclusions. Zircon concentrations in rutile inclusions ranged from 194 to 1340 ppm using inductively coupled

plasma–mass spectrometry. Missouri River sapphire was suggested to form at a higher temperature (~750°C) than Rock Creek sapphire (~660°C). **Dr. Rachelle Turnier** (GIA, Carlsbad) studied sapphire from Myanmar, Madagascar, and Sri Lanka, pairing photoluminescence (PL) spectra and trace element contents. Dr. Turnier observed that Cr^{3+} in sapphire is an efficient luminophore with intense red luminescence emission. Chromium in the corundum lattice can overcome high iron concentration and still cause intense luminescence. For example, 3 ppmw Cr^{3+} and 2500 ppmw Fe^{3+} can still yield luminescence of 1,000,000 counts/s/mW.

Other colored gemstone studies included beryl (oral), tourmaline (oral), and nephrite (poster). **Dr. Rhiana Henry** (Earth, Ocean and Atmospheric Sciences Department, University of British Columbia, Vancouver) investigated structural changes in response to chemical composition variation in beryl ($Be_3Al_2Si_6O_{18}$). Beryl's crystal structure was analyzed using single-crystal X-ray diffraction (XRD), and chemical composition was acquired via electron microprobe analysis (EPMA). She concluded that beryl's crystal structure could be calculated using the average ionic radii of the measured cations at the aluminum site (octahedron site) and the beryllium site (one of the tetrahedron sites). **Dr. Yusuke Katsurada** (GIA, Tokyo) investigated the dominant chromophores (Fe^{2+} and Cu^{2+}) in cuprian Paraíba tourmaline. Oriented wafers were prepared to collect both o-ray and e-ray ultraviolet/visible/near-infrared (UV-Vis-NIR) absorption spectra. Copper and iron concentrations were measured with laser ablation–inductively coupled plasma–mass spectrometry. This study contributes to the simulation of unpolarized UV-Vis-NIR spectrum and the approximation of copper and iron concentrations in cuprian tourmaline. **Ping Li** (Tongji University, Shanghai) demonstrated nephrite's microstructure as an indicator of origin. Nephrite microstructure, including grain size and mineral aggregation, were observed under the petrographic microscope. Nephrites from Xiaomeiling, Maxianshan, and Longxi in China underwent different extents of tectonism and metasomatism.

In recent years, GIA's Research and Development department has broadened its areas of interest, which was demonstrated in two other presentations. **Dr. Matthew Hardman** (GIA, Carlsbad) investigated the capability of machine learning to classify treated/untreated and synthetic/natural gemstones. More than 3,000 PL spectra of diamonds and 500 sets of trace element data of pearls were studied using the Boruta statistical algorithm. This approach identified PL peaks at 67.6, 503.2, 524.3, and 575.0 nm as important in identifying the treatment of CVD lab-grown diamond. Using machine learning, Dr. Hardman confirmed that manganese concentration is significant in identifying seawater or freshwater origin in pearls. **Dr. Sona Taijiryan** (GIA, Carlsbad) presented a poster on the main gem trading routes of the early modern period, from 1500 to 1800 CE. By translating an eighteenth-century manuscript from an Armenian gem merchant in India, Dr. Tajiryan demonstrated the East-West trade routes for the most popular gems in the first half of that century, including Indian diamonds, Southeast Asian rubies and spinels, Colombian emeralds, Sri Lankan pearls, and Mediterranean corals.

Diamonds. **Dr. Evan Smith** (GIA, New York) investigated a 910 ct type IIa diamond from Lesotho to indicate its formation in the mantle. This type of large and highly pure diamond is commonly known as CLIPPIR (Cullinan-like, large, inclusion-poor, pure, irregular) diamond. Inclusions such as cohenite (Fe_3C), troilite (FeS), and metallic Fe-Ni-C-S melt were identified using synchrotron X-ray diffraction at Argonne National Laboratory. The geochemistry of these inclusions confirmed a sublithospheric origin of the host diamond and provided evidence that during the diamond's formation, subduction of basaltic ocean crust to the lower mantle was occurring. **Dr. Mei Yan Lai** (GIA, Carlsbad) shared her recent doctoral research completed at the University of Alberta, which investigated lithospheric mantle composition and volatile recycling in the West African Craton. Inclusion mineralogy, major/trace elemental composition, and carbon/nitrogen host isotopic analyses for 105 diamonds from the Koidu mine in Sierra Leone were systematically analyzed. Dr. Lai indicated two significant and distinct episodes of eclogitic diamond formation in Koidu diamonds: cores precipitated from crustal melts and rims formed from mantle-derived melts.

Other presentations examined diamond in sedimentary systems. In alluvial environments, alpha radiation can cause a green or brown surface color. **Dr. Christopher M. Breeding** (GIA, Carlsbad) reported on his recent study of a rare pink stain in a natural type Ib Fancy brownish yellow diamond, a feature also caused by radiation damage. PL spectroscopy suggested that high concentrations of nitrogen-vacancy (NV^-) defects caused the pink color. It was suspected to have originated as a green diamond that turned pink as a result of higher temperature burial. Also, **Dr. Roy Bassoo** (GIA, Carlsbad) reported on various thermal annealing experiments on natural colorless diamonds to imitate diamond residence in a natural sedimentary system. Nitrogen content and aggregation, defect concentration, and luminescence color response upon heating were studied using Fourier-transform infrared (FTIR) spectroscopy, PL spectroscopy, and optical UV luminescence, respectively. Dr. Bassoo concluded that diamonds in a sedimentary system do not change their bodycolor, but such a system can influence defect-related luminescence.

GIA poster sessions highlighted three interesting colored diamond projects. First, **Sarah Arden**, **Abadie Ludlam**, and **Elina Myagkaya** (GIA, New York) presented their study on etch channels in a 3.17 ct pink type IIa diamond. A profusion of meandering ("worming") channels of various lengths embedded in this pink diamond were observed with micro X-ray computed tomography (CT). High strain was observed under the polariscope, and GR1 defects were mapped as clusters around etch channels using PL. The authors hypothesized two possible formation mechanisms

Figure 28. The GIA booth attracted GSA attendees from all over the world. In the foreground, Nathan Renfro speaks with a visitor. Photo by Cathy Jonathan.

for the etch channels' formation: (1) a type of line defect causing localized strain that is more vulnerable to dissolution and/or (2) Rose channels caused by micro-twinning and subsequently etched by mantle fluids. **Skyelar Caplan** (GIA, New York) reported a new color center (525 nm) as the cause of type Ia Fancy pink diamond. The 525 nm band together with an H-related 835 nm broad band caused a transmission for yellow and green light (610–660 nm) and resulted in a pink color. The 525 nm band observed in the UV-Vis absorption spectrum was related to high nickel content. **Stephanie Persaud** (GIA, New York) investigated two types of color-changing diamonds, chameleon and cryogenic, using spectroscopic analysis. Chameleon diamond changes from grayish green to orangy yellow upon heating, while cryogenic diamond changes from dark gray to light yellow when cooled to freezing temperatures. The cause of color change upon heating/cooling was attributed to changes in energy within the electron band gap.

In addition to the research talks and posters, GIA's booth in the exhibition hall also attracted many visitors. **Robert Weldon** (GIA, Carlsbad) hosted a demonstration of the use of light and camera settings for gemstone photography. He shared the stories and knowledge behind his photographs of the Hope diamond, the Dom Pedro aquamarine, and other notable gems. **Nathan Renfro** (GIA, Carlsbad) demonstrated techniques for inclusion photomicrography (figure 28) using different types of light sources.

An evening reception jointly hosted by GIA and the Mineralogical Society of America was held on October 11. The event provided gemologists and mineralogists with a great opportunity to exchange ideas and facilitate collaboration. In another GSA technical session, **Dr. James Shigley** shared GIA research opportunities with early-career mineralogists and crystallographers. Overall, the 2022 GSA meeting attracted strong attendance and notable interest in the gemology technical sessions and exhibits. We look forward to the 2023 GSA meeting, scheduled for October 15–18 in Pittsburgh, Pennsylvania.

Si Athena Chen, Tao Hsu, and James E. Shigley
GIA, Carlsbad

AUCTION REPORTS

Fall 2022 auction highlights. The astounding results of colored diamond sales in the spring auction season (Summer 2022 GNI, pp. 260–263) left expectations high for fall. Pink diamonds set the scene for the beginning of the season, starting with a bang at a Sotheby's stand-alone sale in Hong Kong in October. Selling for $57.7 million, almost three times its estimate, the 11.15 ct Williamson Pink Star (figure 29) became the second most valuable jewel ever sold at auction. After 20 minutes and 50 bids, the GIA-graded natural Fancy Vivid pink internally flawless cushion-shaped diamond broke the record price per carat for any diamond or gemstone sold at auction, at $5.2 million a carat.

The colored diamond trend headed downward the following month with the Fortune Pink (figure 30) at Christie's Magnificent Jewels sale in Geneva, selling below expectations at the lower end of its estimate. Fetching $28.9

Figure 29. The 11.15 ct Williamson Pink Star is set in an 18K pink and white gold ring, along with 1.41 carats of trapeze-cut diamonds and 0.14 carats of brilliant-cut pink diamonds. Courtesy of Sotheby's.

million, the GIA-graded 18.18 ct stone is the largest pear-shaped Fancy Vivid pink diamond ever sold at auction.

Figure 30. The 18.18 ct Fortune Pink sold in Geneva for $28.9 million. Courtesy of Christie's.

Figure 31. Surrounded by pink diamonds, this 31.62 ct Fancy blue diamond pendant sold within its estimate at $11.8 million. Courtesy of Christie's.

Another pink diamond, a 13.15 ct emerald cut, was slated to lead Christie's December Magnificent Jewels sale in New York before it was withdrawn weeks before the auction and later revealed as alleged stolen property. A 31.62 ct Fancy blue diamond pendant (figure 31) was then placed as the top lot of the auction. The GIA-graded pear modified brilliant cut, noted by Christie's as the largest of its kind to appear at auction, garnered $11.8 million, toward the lower end of the estimate. Three other blue diamonds offered by Sotheby's from the De Beers Exceptional Blue collection drew lackluster results throughout the season. Two were left unsold, and one was withdrawn prior to auction.

In an unexpected conclusion to the season, the Golden Canary (figure 32) sold below its estimate at $12 million. Without a reserve, Sotheby's anticipated the 303.10 ct pear-shaped Fancy Deep brownish yellow diamond to secure more than $15 million in the New York auction. Still, the diamond became the third most valuable diamond ever sold at auction, Sotheby's noted. As the largest flawless or internally flawless and largest pear-shaped diamond graded by GIA to date, the Golden Canary can be traced back to a young girl's discovery of an 890 ct rough near her uncle's house in the Democratic Republic of the Congo in the early 1980s. The 407.48 ct Incomparable, the largest of the 15 finished stones from the rough diamond, was recently transformed into the Golden Canary to improve its color and shape.

The real surprise of Sotheby's New York auction—and perhaps the season—was the sale of a ring featuring a 6.25 ct emerald recovered from the legendary 1622 shipwreck of the *Nuestra Señora de Atocha*. The ring sold in just five minutes for $1.2 million, more than 17 times its estimate. All proceeds were donated to humanitarian efforts in Ukraine.

Erica Zaidman
GIA, Carlsbad

IN MEMORIAM

Peter Keller. *Gems & Gemology* mourns the passing of Dr. Peter Keller (figure 33) on November 8, 2022. Keller dedicated 50 years of his life to the gemological community and made countless contributions to GIA and *G&G*.

Born in 1947 in Allentown, Pennsylvania, Keller became interested in rocks and minerals at an early age. After obtaining his undergraduate degree in geology from George Washington University, Keller earned a master's degree and a PhD in geology and earth science from the University of Texas. Keller began his career as curator of the Gem and Mineral Hall at the Natural History Museum of Los Angeles County before joining GIA as director of education in 1980.

Figure 33. Dr. Peter Keller during his time as director of education at GIA. Photo by GIA.

For more than a decade, Keller was instrumental to *G&G* as an author and as associate editor. In the first half of the 1980s, he wrote several landmark articles documenting his visits to gem deposits worldwide. "Emeralds of Colombia" (Summer 1981) received third place in *G&G*'s annual Most Valuable Article awards. He was a key contributor to *G&G*'s Spring 1986 special issue on China, reporting on the emerging gem resources in various Chinese provinces.

In addition to writing for *G&G*, Keller wrote and published two influential books, *Gemstones and Their Origins* (1990) and *Gemstones of East Africa* (1992). He even ventured into filmmaking earlier in his career, serving as associate producer on a documentary film titled *Gems of the Americas*, which was coproduced by the Natural History Museum of Los Angeles County and GIA.

Keller spent much of his career as president and CEO of the Bowers Museum in Santa Ana, California. He is survived by his wife, children, stepchildren, and grandchildren. We extend our deepest condolences to his family, friends, and colleagues.

Figure 32. The 303.10 ct Golden Canary, recently recut from the Incomparable, became the third most valuable diamond sold at auction. Courtesy of Sotheby's.

ERRATUM

In the Fall 2022 article "Gems on Canvas: Pigments Historically Sourced from Gem Materials," the photos in figures 13, 15, and 20 were credited to the National Gallery of Art in Washington, DC, in error. The photos are courtesy of the National Gallery in London.